



Plume-ridge interaction, lithospheric stresses, and the origin of near-ridge volcanic lineaments

Eric Mittelstaedt and Garrett Ito

School of Ocean and Earth Science and Technology, University of Hawai'i, 1680 East-West Road, Honolulu, Hawaii 96822, USA (staggie@soest.hawaii.edu)

[1] In many hot spot–ridge systems, formation of off-axis volcanic chains or lineaments occurs between the hot spot centers and nearby mid-ocean ridges. In some cases, such as Galápagos, Kerguelen, and possibly the Mid-Pac Mountains and Tristan, these lineaments appear to meet in a focus zone near the hot spot and fan outward in the direction of the ridge axis. The origins of these lineaments are not well known and do not easily fit into typical conceptual models of ridge or hot spot volcanism. It has been proposed for the Galápagos region that such lineaments are caused by channeling of hot asthenosphere from off-axis mantle plumes toward mid-ocean ridges, where enhanced volcanism initiates island formation (Morgan, 1978). Alternatively, other workers suggest that these lineaments are controlled by patterns of stress in the lithosphere. We examine this latter hypothesis by considering the effects of buoyant uplift and asthenospheric shear on the base of the lithosphere induced by an expanding mantle plume. Using thin plate theory, we calculate the two-dimensional (plan view) pattern of depth-integrated stresses in a plate of varying thickness. Both a straight, continuous ridge and a ridge-transform-ridge system are simulated by a displacement discontinuity, boundary element model. Ridge and transform segments have imposed normal and zero shear tractions, and we test different idealized tectonic or far-field stress conditions. Assuming that volcanism is promoted by lithospheric tension and aligns along lineaments parallel to trajectories of least tensile stress, calculations reproduce the rough fan-shaped pattern of lineaments between the Galápagos Archipelago and the Galápagos Spreading Center. The focus of the fan shape is over the plume center when it interacts with a straight ridge, but the fan focus appears closer to a segmented ridge, offset by a transform fault, if the ridge segments are more tensile than the far-field stress. This condition provides a plausible explanation for the apparent focus at the Galápagos north of the hot spot center. The width of the fan pattern along the ridge axis is predicted to increase as the plume-ridge separation increases and as the far-field stress becomes more tensile parallel to the ridge. The observed width along the Galápagos Spreading Center is consistent with a nearly isotropic remote stress. Models predict the lithospheric tension caused by plumes to promote lineament formation on only young lithosphere. In support of this prediction, a compilation of data from 23 hot spots shows that lineament formation is common near hot spots with plume-ridge separations of <1250 km or on lithosphere of <25 Ma, but not on older lithosphere.

Components: 11,534 words, 10 figures, 1 table.

Keywords: Galápagos; hot spot; lithospheric stress field; plume-ridge interaction; volcanic lineaments.

Index Terms: 3035 Marine Geology and Geophysics: Midocean ridge processes; 3037 Marine Geology and Geophysics: Oceanic hotspots and intraplate volcanism; 8164 Tectonophysics: Stresses: crust and lithosphere.

Received 6 October 2004; **Revised** 24 February 2005; **Accepted** 16 March 2005; **Published** 1 June 2005.

Mittelstaedt, E., and G. Ito (2005), Plume-ridge interaction, lithospheric stresses, and the origin of near-ridge volcanic lineaments, *Geochem. Geophys. Geosyst.*, 6, Q06002, doi:10.1029/2004GC000860.

1. Introduction

1.1. Mantle Plume-Ridge Interaction

[2] A well studied form of magmatic process involves hot spot–ridge interaction. Current interactions between at least 21 hot spots and nearby ridges produce geophysical and geochemical anomalies along 15–20% of the global mid-ocean ridge network [Ito *et al.*, 2003]. Geochemical anomalies show variations in noble gas and isotope ratios and trace element concentrations [Detrick *et al.*, 2002; Hanan *et al.*, 1986, 2000; Ito *et al.*, 2003; Keller *et al.*, 2000; Sinton *et al.*, 2003; Taylor *et al.*, 1995]. Geophysical observations demonstrate the presence of elevated topography, negative gravity anomalies [Ito and Lin, 1995; Nadin *et al.*, 1995; Olson, 1990; Richards *et al.*, 1988], and anomalous crustal production [Ito *et al.*, 2003; Sinton, 1992; White *et al.*, 1992]. Together, these observations not only reveal the importance of hot spot–ridge interaction on the structure and composition of the oceanic lithosphere, but they also support the notion that many of these systems involve interaction with mantle plumes.

[3] Manifestations of plume-ridge interaction are found across the ocean basins. Asymmetric spreading and ridge reorientations at many hot spot–ridge systems including Iceland, Kerguelen, the Galápagos, Shona and Louisville [Hardarson *et al.*, 1997; Small, 1995; Wilson and Hey, 1995] suggest changes in large scale plate shape and plate motion [Muller *et al.*, 1998]. Also, formation of volcanic lineaments between off-axis hot spot centers and nearby ridges leads to the creation of new islands and seamounts [Harpp *et al.*, 2003; Harpp and Geist, 2002]. The origin of these lineaments is a poorly understood expression of hot spot–ridge interaction and their presence provides an opportunity to extend our general understanding of asthenosphere-lithosphere dynamics.

1.2. Near-Ridge Lineaments

[4] At many hot spot–ridge systems, volcanic lineaments extend from off-axis hot spots to nearby mid-ocean ridges (Figure 1). Examples include Louisville [Lonsdale, 1988; Small, 1995; Vlastelic *et al.*, 1998], Kerguelen [Small, 1995], Reunion [Dyment, 1998; Morgan, 1978], Tristan de Cuhna, Musicians [Kopp *et al.*, 2003], the Galápagos [Harpp *et al.*, 2003; Harpp and Geist, 2002; Morgan, 1978; Sinton *et al.*, 2003], the Line Islands (Mid-Pac Mountains), and possibly the Discovery and Shona hot spots [Small, 1995].

Morphologies range from continuous ridges at Rodrigues, Hollister, and Genovesa ridges, to aligned but distinct seamounts and islands at the Wolf-Darwin lineament and Tristan de Cunha. Lineaments show arcuate to nearly linear patterns that, in the cases of Galápagos [Sinton *et al.*, 2003], Kerguelen and possibly the Line Islands (Mid-Pac Mountains) and Tristan, fan out toward ridges from a focus zone near the hot spot (Figure 1). Most lineaments of this type occur on young, weak lithosphere and may be the result of magma exploiting the lithospheric stress pattern associated with plume-ridge interaction [Harpp *et al.*, 2003; Harpp and Geist, 2002; Sinton *et al.*, 2003].

1.3. Galápagos Lineaments

[5] Recent studies have focused on the origin and characteristics of off-axis lineaments found near the Galápagos Archipelago [Harpp *et al.*, 2003; Harpp and Geist, 2002]. We focus on the Galápagos region because extensive morphological [Sinton *et al.*, 2003], geochemical [Cullen and McBirney, 1987; Detrick *et al.*, 2002; Geist *et al.*, 1986, 1999; Harpp *et al.*, 2003; Harpp and Geist, 2002; Schilling *et al.*, 2003; Sinton *et al.*, 1996], and geophysical investigations [Canales *et al.*, 1997; Feighner and Richards, 1994; Ito *et al.*, 1997; Schubert and Hey, 1986; Werner *et al.*, 2003; Wilson and Hey, 1995] provide better constraints on models of lineament formation than currently possible at other hot spot systems.

[6] A series of approximately seven volcanic chains arrayed in a distinctly fan-shaped pattern, emanate from a focal zone just north of Santiago Island [Sinton *et al.*, 2003] toward the Galápagos Spreading Center (GSC) between $\sim 92^{\circ}30'W$ and $89^{\circ}W$ (Figure 1a). The majority of these volcanic lineaments are concave toward the GSC and curve to meet the ridge at nearly right angles both to the west and east of the large (~ 100 km offset) transform at $91^{\circ}W$ [Sinton *et al.*, 2003]. Many researchers have speculated as to the origin of the most prominent of these volcanic chains, the Wolf-Darwin Lineament (WDL). Originally, Morgan [1978] proposed that Wolf and Darwin Islands near Galápagos and Rodrigues Island near Reunion are examples of “a second type of hot spot island,” formed by an asthenospheric channel connecting the off-axis hot spots to the ridge axis. Enhanced volcanism at the intersection of the channel and the ridge creates seamounts and islands which are subsequently rafted away by plate motion. This hypothesis predicts that ages along the lineaments should increase away from the ridge, equal to the

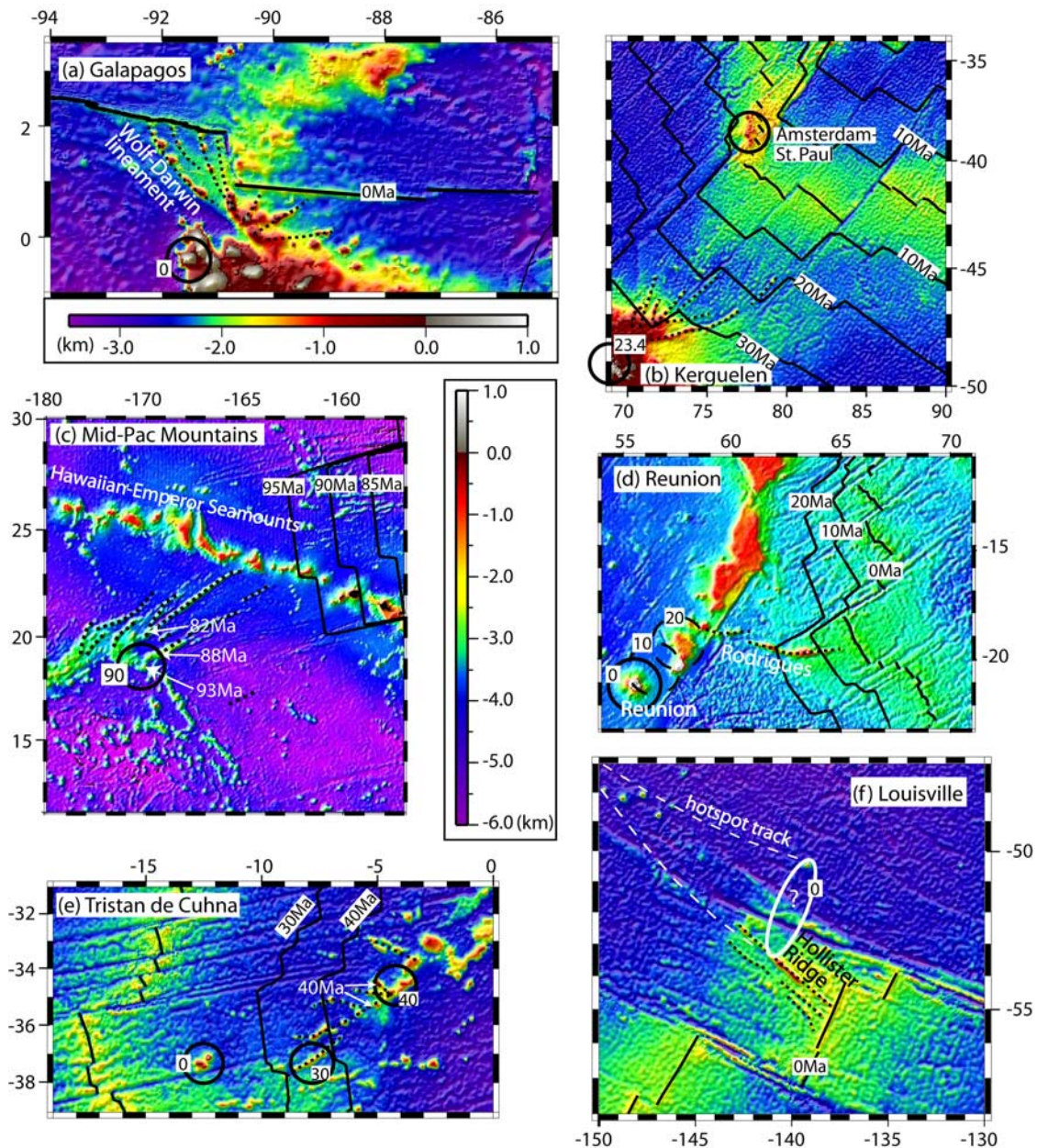


Figure 1. Volcanic lineaments are seen at several hot spots, including (a) the Galápagos, (b) Kerguelen, (c) Line Islands/Mid-Pacific Mountains, (d) Reunion, (e) Tristan de Cuhna, and (f) Louisville (white dashed lines and ellipse indicate possible hot spot track and current plume center locations). Predicted bathymetry from satellite altimetry [Smith and Sandwell, 1997]. Seamount ages, plume locations, and plate reconstructions from Coffin *et al.* [2002], Davis *et al.* [2002], Geli *et al.* [1998], Muller *et al.* [1997], O'Connor and Roex [1992], O'Connor and Duncan [1990], and Wessel and Kroenke [1998]. Black circles indicate the approximate center of volcanism at the labeled times (Ma). Seafloor isochrons show approximate mid-ocean ridge geometries at the labeled times. Plume-ridge separation is the distance between the circles and the ridge at the appropriate age.

age of the underlying crust. Volcanic rocks sampled on the WDL, however, do not reveal this simple age progression and lineament ages are 1–5 m.y. younger on the WDL [Sinton *et al.*, 1996; White *et al.*, 1993] and 10–15 m.y. younger on

Rodrigues [Bonneville *et al.*, 1988] than Morgan [1978] predicts. The gravity analysis of Feighner and Richards [1994] suggests that the WDL occurs near the boundary of a discontinuity in effective elastic plate thickness where a lithospheric fault

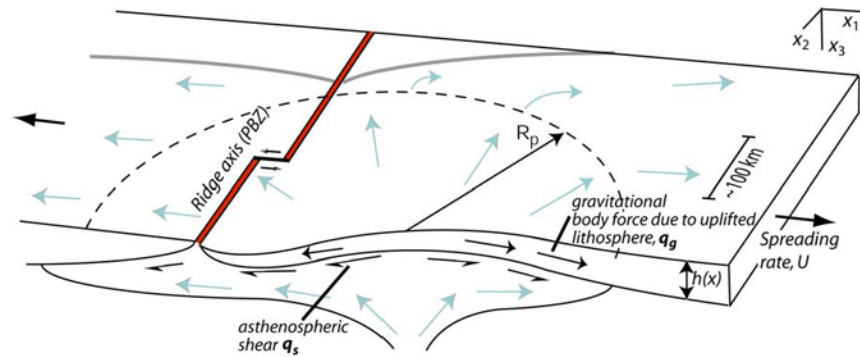


Figure 2. Conceptual model. Red line along the ridge axis represents the plate boundary zone (PBZ) of magmatism and nonelastic deformation, with arrows showing sense of motion across the transform fault. Anomalous buoyant (mantle plume) asthenosphere uplifts the plate, causing plate parallel gravitational forces (q_g). Large arrows show flow of buoyant asthenosphere, which introduces shear along the base of the plate q_s . R_p denotes extent over which plume flow is assumed to remain nearly radial. At radii greater than this, plume flow deviates due to plate motion. Both plume uplift and asthenospheric shear introduce tension in the plate.

may have occurred allowing magma to reach the surface.

[7] Influence of the 91°W transform fault on lineament formation is suggested by the systematic decrease in lineament trend [Sinton *et al.*, 2003] and decrease in curvature as the lineaments approach the transform. Harpp and Geist [2002] and Harpp *et al.* [2003] hypothesize that the WDL and Genovesa ridge are consequences of lithospheric tension associated with the 91°W transform fault along the GSC. The transform model proposed by Harpp and Geist [2002], however, predicts a lineament curvature opposite to that observed and increasing curvature near the transform corner [see Gudmundsson, 1995]. Alternatively, Sinton *et al.* [2003], suggest that plate parallel gravitational stresses due to lithospheric uplift from an impinging plume will produce a radial pattern of least tension promoting radial dike orientations [Ernst and Buchan, 1997]. This hypothesis predicts the radiating volcanic lineaments to be straight rather than curved and, as noted by Sinton *et al.* [2003], predicts them to radiate from the center of the plume whereas the Galápagos lineaments radiate from an area on the northern edge of the archipelago. Both the prediction of transform-induced stresses and plume-induced stresses individually fail to adequately explain the formation of the Galápagos lineaments. We propose that lithospheric stresses due to the combined effects of the plume and segmented ridge can explain the general lineament pattern, focus location, and decreasing curvature near the transform fault.

[8] The goal of this paper is to explore how hot spot–ridge interaction can influence the lithospheric stress field and thus the pattern of volcanic lineaments. Our study includes quantitative tests of the hypotheses of Harpp *et al.* [2003], Harpp and Geist [2002] and Sinton *et al.* [2003]. We assume that the aforementioned hot spot–ridge systems involve buoyant asthenosphere rising and spreading beneath the lithosphere. In this context we refer to these interactions as “plume”–ridge interactions. We calculate two-dimensional (2-D), plan view, depth-integrated stresses in a plate of varying thickness subject to loads due to plume shear, plate parallel gravitational body forces and boundary tractions along both a straight ridge and a ridge-transform-ridge system. On the basis of the model results, we address the implications for near, but off-ridge volcanism for the particular case of the Galápagos as well as other oceanic hot spots.

2. Conceptual and Mathematical Model

2.1. Conceptual Model

[9] Figure 2 illustrates our conceptual model of forces involved in plume–ridge interaction. We approximate the lithosphere as an elastic plate and treat the zone of rifting near the ridge axis and the region of strike-slip motion along transform faults as an internal boundary. We refer to this region of nonelastic deformation along the ridge as the plate boundary zone, PBZ (Figure 2). The pattern of stress in the plate is a sum of all forces

acting on the plate. These forces include tractions along the PBZ and the distal plate boundaries, the pull of gravity on surface topography (which includes the deepening with seafloor age) as well as asthenospheric shear on the base of the plate [Forsyth and Uyeda, 1975]. Indeed the state of stress near mid-ocean ridges varies from region to region, ridge to ridge (J. Reinecker et al., The 2004 release of the World Stress Map, available at <http://www.world-stress-map.org>). To make our models general and to focus on the local effects of plume-ridge interaction, we simplify the effects of all of the distal forces as a uniform far-field stress and then calculate the perturbations caused by plume-ridge interaction. First, we consider a case of isotropic far-field stress equal in magnitude to the normal stress (either tensile or compressive) on the ridge. Ridge-normal compression could be caused by the excess morphological high at the ridge axis while ridge-normal tension could be caused by seafloor spreading and is evident by extensive normal faulting in the PBZ. Second, we illustrate the effects of a nonisotropic far-field stress. Finally, we consider a PBZ stress that is more tensile than the far-field isotropic stress.

[10] Locally, the stress pattern near a plume-affected ridge will be perturbed by plume-induced stresses. The plume-induced loads on the plate are excess asthenospheric shear (\mathbf{q}_s , bold terms denote vector quantities), caused by buoyant asthenospheric material (mantle plume) spreading radially beneath the lithosphere, and the pull of gravity (\mathbf{q}_g) down the slope of the anomalously uplifted lithosphere [Westaway, 1993]. The combination of these loads creates horizontally varying lithospheric stresses. We assume magma will penetrate the lithosphere and erupt along lineaments parallel to the direction of least tensile resultant stress, as integrated through the thickness of the plate.

2.2. Mathematical Method

[11] The lateral extent of the lithosphere is large compared to its thickness; therefore we use thin shell theory to develop our 2-D governing equations of an elastic plate. To describe stresses in the plate, we use nonlithostatic, depth-integrated stresses, or stress resultants, N_{ij} (see Appendix A),

$$N_{ij} = \int_0^h \sigma_{ij} dx_3 \quad (1)$$

($i, j = 1, 2$ for the lateral directions), where σ_{ij} are stresses throughout the lithosphere, h is lithosphere thickness, and x_3 is the vertical axis corresponding

to depth in our model where $x_3 = 0$ is the surface of the plate (Figure 2).

[12] Strictly, the reference state of the lithosphere is a curved “shell” due to the deepening of mantle isotherms with the square root of distance from the ridge, however, scaling arguments show that a flat plate provides a good approximation for our problem (see Appendix A). For a flat plate of uniform thickness, equilibrium is solved by a balance of laterally varying stress resultants, N_{ij} , and plume-induced loads, which behave mathematically as body forces ($\mathbf{q} = \mathbf{q}_s + \mathbf{q}_g$)

$$\frac{\partial N_{ij}}{\partial x_i} + q_j = 0 \quad (2)$$

(summation over i is implied). The constitutive relation of stress resultants to strain along the mid-plane of the plate (ε_{ij}) is given by Novozhilov [1959]

$$\begin{bmatrix} N_{11} \\ N_{22} \\ N_{12} \end{bmatrix} = \begin{bmatrix} Eh(1-\nu^2)^{-1} & E\nu(1-\nu^2)^{-1} & 0 \\ E\nu(1-\nu^2)^{-1} & Eh(1-\nu^2)^{-1} & 0 \\ 0 & 0 & Eh(1+\nu)^{-1} \end{bmatrix} \cdot \begin{bmatrix} \varepsilon_{11} \\ \varepsilon_{22} \\ \varepsilon_{12} \end{bmatrix}, \quad (3)$$

where E is Young’s modulus and ν is Poisson’s ratio (see Table 1 for values used). The compatibility relation is [Novozhilov, 1959]

$$(1-\nu) \left[\frac{\partial^2 N_{11}}{\partial x_2^2} + \frac{\partial^2 N_{22}}{\partial x_1^2} \right] - \nu \left[\frac{\partial^2 N_{22}}{\partial x_2^2} + \frac{\partial^2 N_{11}}{\partial x_1^2} \right] = 2 \frac{\partial^2 N_{12}}{\partial x_1 \partial x_2} \quad (4)$$

and when combined with (2) yields

$$\nabla^2(N_{11} + N_{22}) = -\frac{1}{(1-\nu)} \left[\frac{\partial q_1}{\partial x_1} + \frac{\partial q_2}{\partial x_2} \right]. \quad (5)$$

[13] Lithospheric cooling increases plate thickness, h , perpendicular to the ridge and ridge segmentation introduces age discontinuities across the fracture zones. For laterally varying elastic parameters ($Eh(x_1, x_2)$) the equations of equilibrium and compatibility can be expressed as (see Appendix B)

$$\frac{\partial \bar{\sigma}_{ij}}{\partial x_i} + b_j = 0 \quad (6)$$

Table 1. Model Parameters

Parameter	Description	Value	Units
b_i	total loads on the plate	-	N
E	Young's Modulus	7×10^9	Pa
ϵ_{ij}	strain	-	-
G	shear modulus	3×10^{10}	Pa
h	plate thickness	-	m
h_p	plume flow thickness	-	m
κ	thermal diffusivity	1×10^{-6}	m^2/s
L	1/2 width of lineament extent along ridge axis	-	m
N_{ij}	stress resultants	-	GN/m
q_s	load due to plume shear	-	N
q_g	load due to gravitational body forces	-	N
q	total load on the plate due to the plume	-	N
r	radial distance from plume center	-	m
R_p	radius of radially dominated plume flow	3.5×10^5	m
u	velocity of plume spreading	-	m/s
x_p	plume-ridge separation distance	-	m
x_1, x_2, x_3	coordinate directions	-	-
μ	viscosity	$10^{18} - 10^{19}$	Pa s
$\Delta\rho$	density deficit of plume material	20	kg/m^3
$\bar{\sigma}_{ij}$	average stress	-	Pa
ν	Poisson's ratio	0.25	-
ΔN_f	$(N_{f11} - N_{f22})$, far-field differential stress	-	GN/m
ΔN_p	$(N_{p11} - N_{p22})$, plume differential stress	-	GN/m

and

$$(1 - \nu) \left[\frac{\partial^2 \bar{\sigma}_{11}}{\partial x_2^2} + \frac{\partial^2 \bar{\sigma}_{22}}{\partial x_1^2} \right] - \nu \left[\frac{\partial^2 \bar{\sigma}_{22}}{\partial x_2^2} + \frac{\partial^2 \bar{\sigma}_{11}}{\partial x_1^2} \right] = 2 \frac{\partial^2 \bar{\sigma}_{12}}{\partial x_1 \partial x_2}, \quad (7)$$

respectively. Combining (6) and (7) yields the single governing equation

$$\nabla^2 (\bar{\sigma}_{11} + \bar{\sigma}_{22}) = - \frac{1}{(1 - \nu)} \left[\frac{\partial b_1}{\partial x_1} + \frac{\partial b_2}{\partial x_2} \right]. \quad (8)$$

In (6)–(8), $\bar{\sigma}_{ij}$ ($= N_{ij}/h$) are depth-averaged stresses and b_i are the combined loads due to uplift and plume shear, q , as well as “fictitious” body force terms arising due to lateral changes in h (see Appendix B)

$$b_i = \frac{q_i}{h} + \frac{\partial h}{\partial x_j} \frac{\bar{\sigma}_{ij}}{h} \Big|_{i \neq j} + \frac{\partial h}{\partial x_i} \frac{\bar{\sigma}_{ii}}{h}. \quad (9)$$

The form of equations (6)–(8) is identical to the equations of plane stress and allows solutions to be found using an Airy stress function formulation.

[14] At straight ridge axes, lithospheric thickness is assumed to vary only perpendicular to the ridge and as such, the fictitious body forces will only include terms with gradients of h in the ridge normal direction (x_1). Near a transform, gradients

in thickness parallel and perpendicular to the ridge axis will exist. Though (8) and (9) are formulated in terms of mean stress, $\bar{\sigma}_{ij}$, we will show results in terms of depth-integrated stresses, or stress resultants, N_{ij} .

2.3. Plume Forces, Lithospheric Strength, and Plate Boundary Conditions

[15] In our model, loads are introduced by the buoyant plume asthenosphere and along the ridge PBZ. These loads generate the local stress pattern. The loads introduced by the plume on the lithosphere, q , include plume shear, q_s , and the plate-parallel pull of gravity due to plate uplift, q_g . In order to calculate q , we approximate the plume spreading beneath the plate as an axisymmetric viscous gravity current.

[16] The flow of plume material near a ridge is controlled by plate-driven corner flow, gravity-driven plume expansion and flow along the slope of the lithosphere [Ribe, 1996]. For simplicity, we restrict consideration to the axisymmetric buoyant “self spreading” term of the equation described by Ribe [1996]. Thus the radius of our plume is not the full extent of the plume beneath the lithosphere or along the ridge axis, but the region where axisymmetric flow dominates (Figure 2). Outside of this radial zone, plume

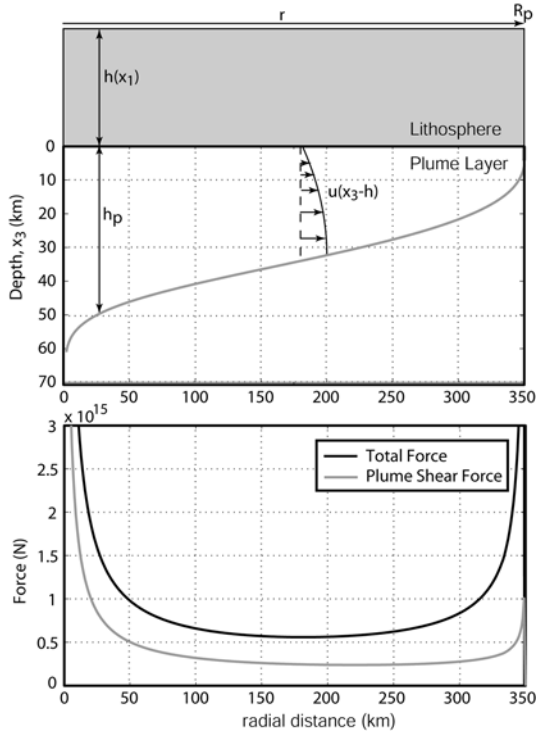


Figure 3. (top) Cross-sectional view of the model plume flow beneath the lithosphere (here sketched with constant thickness). Velocity with depth in the plume is zero immediately beneath the lithosphere and increases to tens of cm/yr at the base of the plume layer. (bottom) On average the plume shear force (q_s , gray) is approximately 40% of the total force (q , black) exerted on the lithosphere due to plume shear and uplift. Large forces at $r = 0$ and $r = R_p$ are consequences of theoretical singularities in the plume solution and are calculated at these locations using an approximate solution [Huppert, 1982].

flow departs from axisymmetry, but the flow is slower than in the radial zone and is not considered here.

[17] To compute q_s we must determine the vertical velocity gradient of plume-flow beneath the lithosphere. Conservation of momentum for a thin layer of fluid yields the solution for radial flow, u , as a function of radial distance from the center of the flow, r , and depth below the lithosphere ($x_3 - h$) [Huppert, 1982]

$$u(r, x_3, t) = -\frac{1}{2} \frac{\Delta \rho g}{\mu} \frac{\partial h_p}{\partial r} (x_3 - h) [2h_p - (x_3 - h)], \quad (10)$$

where g is the acceleration due to gravity, $\Delta \rho$ is the density contrast between the plume and surrounding mantle, h_p is the thickness of the plume flow and μ is dynamic viscosity (Figure 3).

The shear along the base of the plate is found to be

$$q_s = \mu \left. \frac{\partial u}{\partial x_3} \right|_{(x_3-h)=0} = -\frac{1}{2} \Delta \rho g \frac{\partial h_p}{\partial r} 2h_p \quad (11)$$

and is proportional to $(h_p^2/2)$ (Figure 3). Huppert [1982] shows that the equations describing conservation of mass and momentum in a thin layer of fluid can be formulated into a single, second order, ordinary differential equation describing the shape of the flow, $h_p(r)$ [Huppert, 1982, equation (2.25)]. We solve this equation for $h_p(r)$ and $\partial h_p/\partial r$ (in (10) and (11)) using a second-order Runge-Kutta method.

[18] Anomalous buoyant plume material beneath the lithosphere will also produce topographic uplift, the slope of which causes plate parallel gravitational forces. If the radius of the plume is large compared to the flexural wavelength, the height of isostatic topography, h_t , depends on the product of the plume thickness, $\Delta \rho$, and the difference between the mantle density, ρ_m , and the ocean density, ρ_w :

$$h_t = \frac{\Delta \rho}{(\rho_m - \rho_w)} h_p. \quad (12)$$

The plate-parallel gravitational body force due to plate uplift (q_g) is proportional to h_t and the slope of the lithosphere, $\partial h_t/\partial r$,

$$q_g = \frac{\partial h_t}{\partial r} (\rho_l - \rho_w) g h, \quad (13)$$

where ρ_l is lithospheric density. The total plume force is $q = q_s + q_g$ (Figure 3).

[19] In order to understand the response of the lithosphere to the imposed forces, we calculate depth-integrated tensile yield strength (Figure 4). As commonly done, the lithosphere is assumed to behave in a brittle fashion at shallow depths and transition to ductile behavior with depth [Buck and Poliakov, 1998; Chen and Morgan, 1990; Shaw and Lin, 1996]. We assume a two-layer lithosphere with a top layer of basaltic crust having a lower ductile strength than the underlying peridotite mantle [e.g., Shaw and Lin, 1996]. Thickening of the lithosphere is controlled by a half-space cooling model [e.g., Parsons and Sclater, 1977]. A cooling plate strengthens with age, but like Small [1995], we predict the integrated strength to increase gradually at young plate ages ($< \sim 1.8$ m.y. for a crustal thickness of 10 km), when the crust is supplying most of the strength, and to increase more rapidly

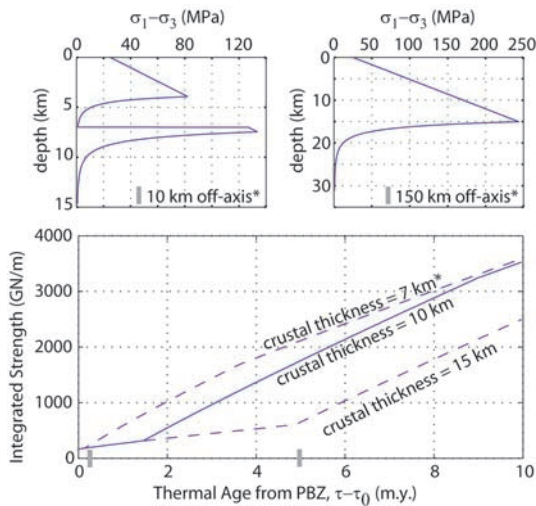


Figure 4. (top) Lithospheric strength envelopes at 10 and 150 km from the ridge axis demonstrate the strength of the lithosphere with depth for a 7 km thick crust. (bottom) Integrated strength of the lithosphere increases with thermal age τ of the lithosphere outside of the PBZ. In young lithosphere the ductile strength dominates the lower crust, while in older lithosphere, brittle behavior is most important. Left side of diagram ($\tau - \tau_0 = 0$) corresponds to the edge of the PBZ, assumed to have cooled as an infinite half-space to a thermal age of $\tau_0 = 0.5$ m.y.

at greater plate ages when the mantle begins to supply strength (Figure 4). Another interesting prediction is that thicker crust will produce a weaker lithosphere which, in turn, may influence the maximum plume-ridge separation distance where lineament formation is possible. When including the transform fault in our models, the strength variations due to the age discontinuity across the transform and fracture zone are present for the entire length of the model.

[20] The boundary conditions include imposed stress resultants in the far field and along the ridge axis. The imposed far-field (resultant) stresses may be tensile or compressive and are assumed to be caused by all of the loads on the plate, except by the local forces associated with plume-ridge interaction. The local ridge axis is subject to imposed normal tractions equal to the value of the far-field stress perpendicular to the ridge. We assume that extension and accretion in the PBZ prevent any substantial shear stress and therefore impose a zero shear stress condition at the ridge axis. For a segmented ridge offset by a transform fault, the normal and zero shear stress conditions are identical along both the ridge and transform segments. Although shear may be present along the transform

at the Galápagos, it does not significantly affect our model solutions.

2.4. Numerical Implementation

[21] Stress resultants are calculated throughout the plate by solving equation (8) with the right hand side approximated by point loads. The well known problem of calculating stress in an infinite plate due to a directed point force is known as Kelvin's problem [Barber, 2002; Crouch and Starfield, 1983; Timoshenko and Goodier, 1934]. We use a plane stress solution of Kelvin's problem to calculate the effect of plume shear and uplift at any given point in the model space. By summing Kelvin solutions due to the appropriate forces at each location, we simulate the effect of the whole plume on the lithosphere.

[22] The boundary conditions along the PBZ are implemented using a displacement discontinuity, boundary element model [Crouch and Starfield, 1983]. The boundary elements method is used for effective modeling of crack-like behavior of the ridge. We begin with an idealized case of a straight ridge axis and extend the ridge well beyond the region of interest (i.e., 10 times the plume radius in both directions) to minimize the influence of the ridge ends on the solutions.

[23] With the Kelvin point forces (imposing the loads q) and the ridge boundary condition applied, we solve equation (8) using an Airy stress function approach to yield a first approximation to N_{ij} and b_i with the "fictitious" body forces initially set to zero. Achieving the final solution requires several iterations over the whole domain to accurately solve for the "fictitious" body forces due to the varying plate thickness (equation (9) and Appendix B). With each successive iteration, the difference between the previous and new stress fields diminishes indicating convergence toward the solution. A solution is assumed to be sufficiently accurate when the difference between successive iterations is less than 0.1% of the maximum stress in the plate.

3. Results

3.1. Straight Ridge

[24] To provide an intuitive understanding of our results we show a series of solutions with the different plate loads sequentially added to the models (Figure 5). For each model, we set a plume volume flux of $90 \text{ m}^3/\text{s}$ [Ribe and Delattre, 1998],

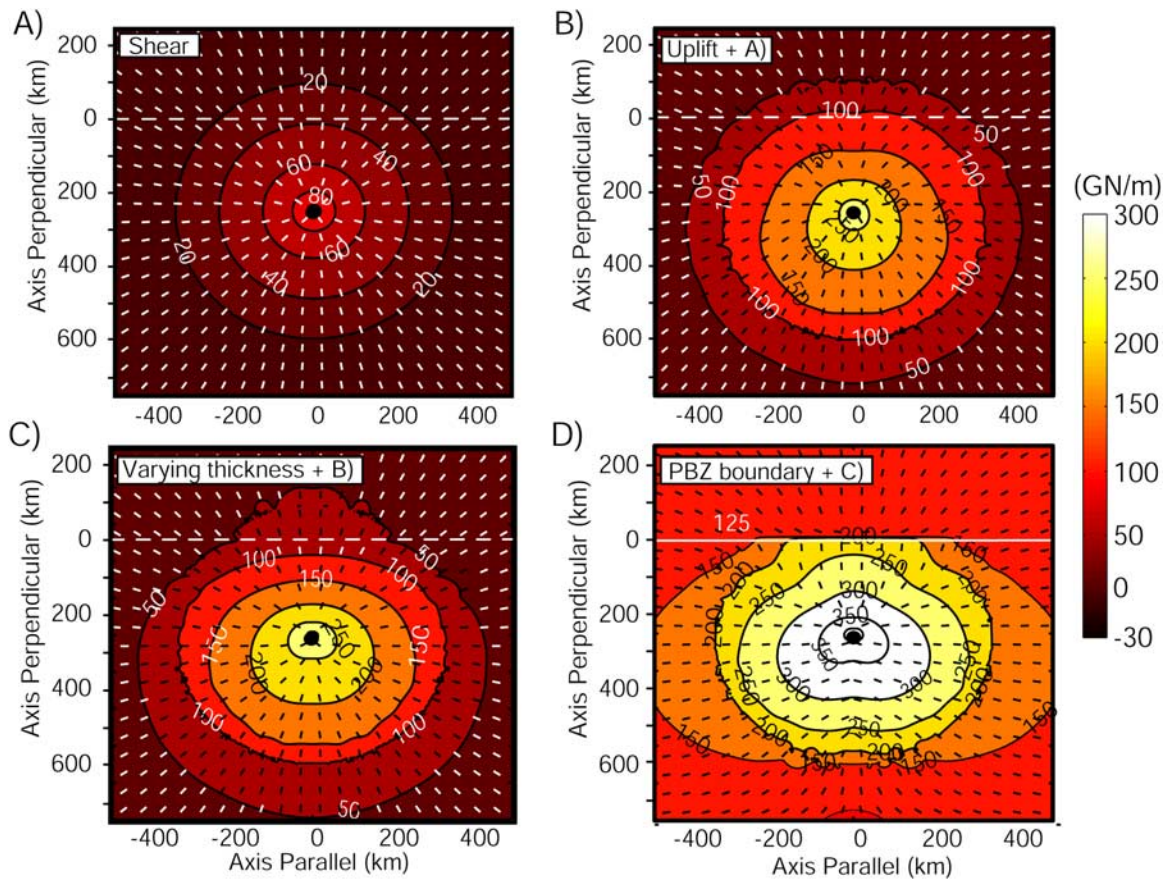


Figure 5. Calculated solutions are due to several components of plume-ridge interaction, shown with different plate loads sequentially added to the model. (a) The axisymmetric shear due to plume flow q_s , (b) plus the gravitational body forces due to dynamic topography q_g , (c) plus the effects of varying plate thickness (see equation (9)), (d) plus the ridge boundary condition. Contours are most tensile stress resultant (GN/m), and ticks are stress trajectories of the least tensile stress resultant. The plume center is denoted by a black dot. Dotted white lines denote the future location of the ridge, while the solid white line in Figure 5d denotes the implemented ridge boundary.

a seafloor spreading rate of 30 km/myr, a radius of axisymmetric plume flow of 350 km, and a plume density deficit appropriate for a temperature excess from local mantle of 200 K. Complete model parameters and variables are described in Table 1. First, we consider a plate with uniform thickness, no ridge axis, zero far-field stress and subject only to the shear due to radial plume expansion. Stress resultants due to plume shear alone show a radial pattern of least tensile stress resultant trajectories with most tensile magnitudes being proportional to $(h_p^2/2)$ and having a maximum at the plume center (Figure 5a). Trajectories of least tensile stress resultants may control the preferred paths of lateral magma propagation through the lithosphere (e.g., dikes will tend to open in the direction of maximum tension) while stress resultant magnitudes are likely to influence the ability of magma to penetrate the lithosphere. Plume shear induces $\sim 40\%$ of the imposed stress due to plume-lithosphere inter-

action (Figure 3). Next we add the effects of topographic uplift (Figure 5b). Plate parallel gravitational body forces due to dynamic topography introduce the remaining $\sim 60\%$ of the stress resultant magnitude. The magnitude of plate parallel gravitational forces is proportional to lithospheric thickness and height of uplift (equation (13)). The thinning of the lithosphere toward the ridge axis therefore produces a nonaxisymmetric pattern of stress resultants with deviation from the radial pattern greatest where gradients in lithospheric thickness are largest.

[25] Adding the effects of variations in plate thickness causes the orientations of least tensile stress resultants to rotate toward the gradient in plate thickness (i.e., toward a ridge axis; Figure 5c) and increases the magnitude of the most tensile stress by $\sim 10\%$. Finally, introduction of an isotropic far-field tension and a ridge boundary, equal to the

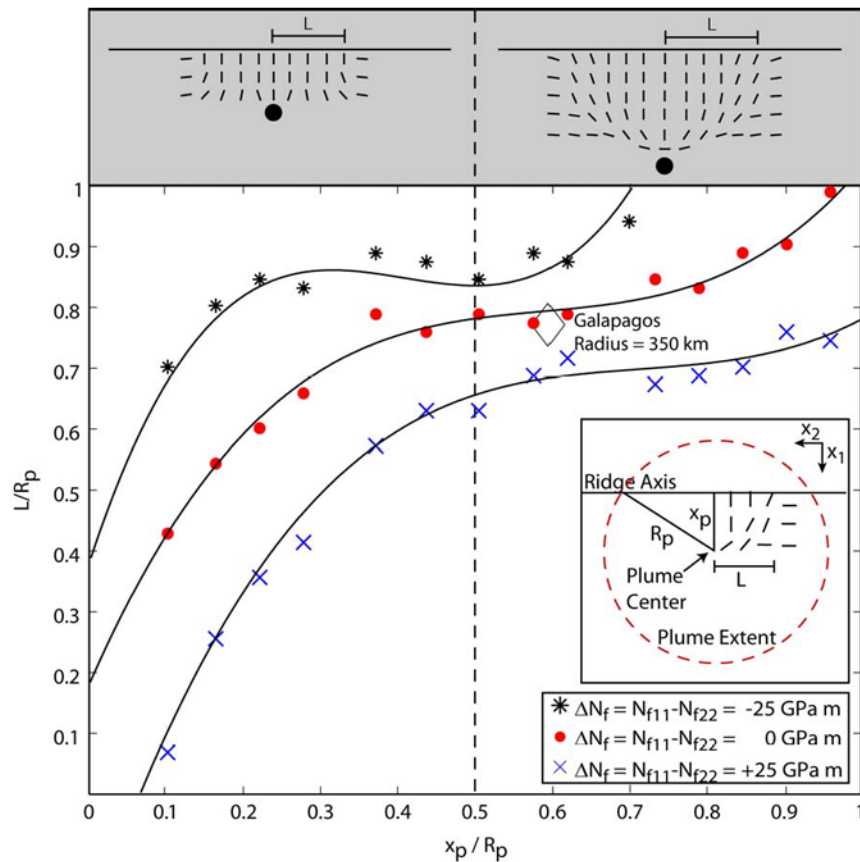


Figure 6. Model predictions of normalized lineament half-width, L/R_p , increase with normalized plume ridge separation, x_p/R_p , and differential far-field stress resultant ($\Delta N_f = N_{f11} - N_{f22}$). The predicted pattern of least tensile stress trajectories forms a fan-shaped pattern for x_p/R_p greater than 0.5. For smaller plume-ridge separations the trajectories maintain ridge perpendicular orientations between the ridge and plume center. Solid curves are best fit cubic functions, which are shown to emphasize the general trends of the model predictions.

far-field condition, increases tension uniformly throughout the plate. The zero shear stress (resultant) condition on the ridge tends to orient least tensile trajectories perpendicular to the ridge. In the area between the plume and the ridge, the stress resultant trajectories form a fan shape with a center slightly ridgeward of the plume and curve to meet the ridge at nearly right angles (Figure 5d).

[26] Ultimately, the extent and shape of the trajectory pattern is produced by the combination of the above forces. When the differential stresses caused by the far-field and ridge conditions are small, the stress pattern is dominated by the axisymmetric plume forces and displays a fan shape. Such conditions are maintained while the differential far-field stress is small or zero, the plume-ridge separation is relatively large ($x_p/R_p > 0.5$), and when the normal stress on the ridge is equal to the far-field stress (Figure 5). Making the ridge and far-field conditions more

tensile or compressive does not change the pattern of stress trajectories, but simply adds uniformly to the stress field.

[27] Variations in the pattern of least tensile stress trajectories with x_p and with the imposed differential far-field stress resultants ($\Delta N_f = N_{f11} - N_{f22}$; see Figure 6) can be characterized by predictions of L , the half-width along the ridge axis that lineaments will intersect the ridge axis at an angle greater than 45° (Figure 6, inset). Values of L normalized by R_p increase with normalized separation (x_p/R_p). At small separations ($x_p/R_p < \sim 0.4$) the increase in width is rapid, at intermediate separations ($\sim 0.4 < x_p/R_p < \sim 0.6$) the increase is more gradual, and for larger separations ($x_p/R_p > \sim 0.6$) width increases again rapidly with separation. Increasing the relative far-field tension perpendicular to the ridge (ΔN_f) roughly preserves the dependence on normalized separation, but shifts the curve to smaller normalized widths (crosses,

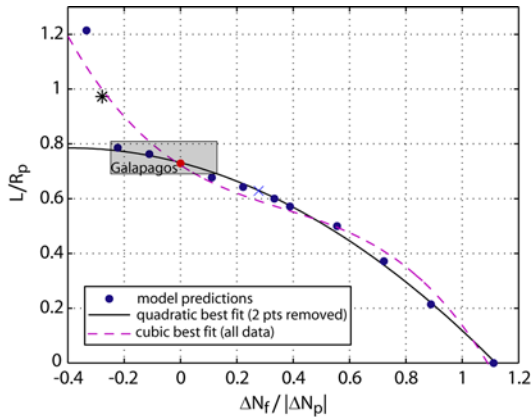


Figure 7. Model predictions of lineament half-width (see Figure 6), L , versus the ratio of the differential remote stress resultant ($\Delta N_f = N_{f11} - N_{f22}$) and the magnitude of the differential plume stress resultant, ΔN_p , 30 km south of the ridge axis between the plume center and ridge in a calculation with $N_{f11} = N_{f22} = 0$. The width of the fan-shaped region diminishes as $\Delta N_f/|\Delta N_p|$ increases. For a plume ridge separation distance, x_p/R_p , of 0.7, most of the model predictions are well approximated by a quadratic fit, but a cubic fit is necessary to fit the total range of predictions. Using measurements of the Galápagos lineaments, the stress regime near the GSC falls within the gray box (see text for details). The black star, red dot, and blue cross correspond to symbols in Figure 6.

Figure 6). Decreasing ΔN_f to negative values reduces the normalized widths (asterisks, Figure 6).

[28] The dependence of normalized width on the differential far-field stress resultant is better illustrated in Figure 7. Here we show L/R_p at $x_p/R_p = 0.72$ and vary ΔN_f normalized by the differential stress resultants due to plume-induced forces in the absence of the ridge and far-field conditions (taken 30 km south of the ridge axis), ΔN_p . For increasing values of $\Delta N_f/|\Delta N_p|$, L/R_p decreases until all least tensile trajectories are ridge parallel at $\Delta N_f/|\Delta N_p| = 1.1$. This decrease in L/R_p with differential far-field stress is well modeled by a quadratic relationship over the majority of far-field conditions. With negative values of $\Delta N_f/|\Delta N_p|$, all trajectories eventually become axis-perpendicular, causing L to increase rapidly with decreasing $\Delta N_f/|\Delta N_p|$ and deviate from the quadratic best-fit line (Figure 7, leftmost points).

3.2. Segmented Ridge

[29] Finally, we test the importance of a transform fault. Transform faults have significant effects on the near-ridge lithospheric stress field [Behn *et al.*,

2002; Pollard and Aydin, 1984] and the 91°W transform fault along the GSC is an example of large scale segmentation that may affect the lineament pattern. We model a transform fault 125 km in length located north of the plume center. The lengths of the two ridge segments are limited to ~ 400 km which is the approximate distance of the next set of transform faults of the GSC to the east and west. Lithospheric thickness is discontinuous across the transform fault throughout the model domain (i.e., we assume the fracture zone extends across the whole model).

[30] First we look at the solutions for a ridge with normal tension equal to the isotropic far-field stress. Stress resultants due solely to the far-field and ridge boundary conditions are isotropic without the plume forces (Figure 8a). With forces due to a plume of viscosity 10^{18} Pa s, a focus zone of least tensile stress trajectories is seen south of the lower transform corner and rideward of the plume center, but is poorly defined (Figure 8c). Trajectory orientations deviate from the general fan-shaped pattern in the inside corner of the transform. With the larger plume viscosity of 10^{19} Pa s, a focus is apparent near the plume center, while the inside corner region again displays trajectories that deviate from the fan-shaped pattern (Figure 8d).

[31] Next we examine solutions where the normal tension along the ridge is greater than the far-field stress by 100 GPa m. As in the previous case, we first examine the effect of the far-field and ridge conditions alone. Trajectories radiate from a distinct focus zone just south of the lower ridge-transform intersection and curve back toward the ridge axis. Near the left (west) side of the transform, the strike of the stress resultant trajectories is nearly parallel to the transform fault and rotates clockwise with distance from the transform (Figure 8b). Stress resultant magnitudes are highly tensile close to the transform, but become compressive south of the transform tip. Inclusion of a plume produces stress resultant magnitudes that are more tensile throughout the plate, reduces the compressive stress south of the transform tip, and produces a general fan-shaped pattern of least tensile stress trajectories (Figures 8d and 8f). With a plume viscosity of 10^{18} Pa s, the apparent trajectory focus zone remains identical to that without plume forces, but the stress trajectories to the left of the transform rotate counterclockwise with increasing distance from the transform; in the opposite sense of the trajectories without the plume forces (Figure 8d). With a larger plume viscosity of 10^{19} Pa s, the apparent focus

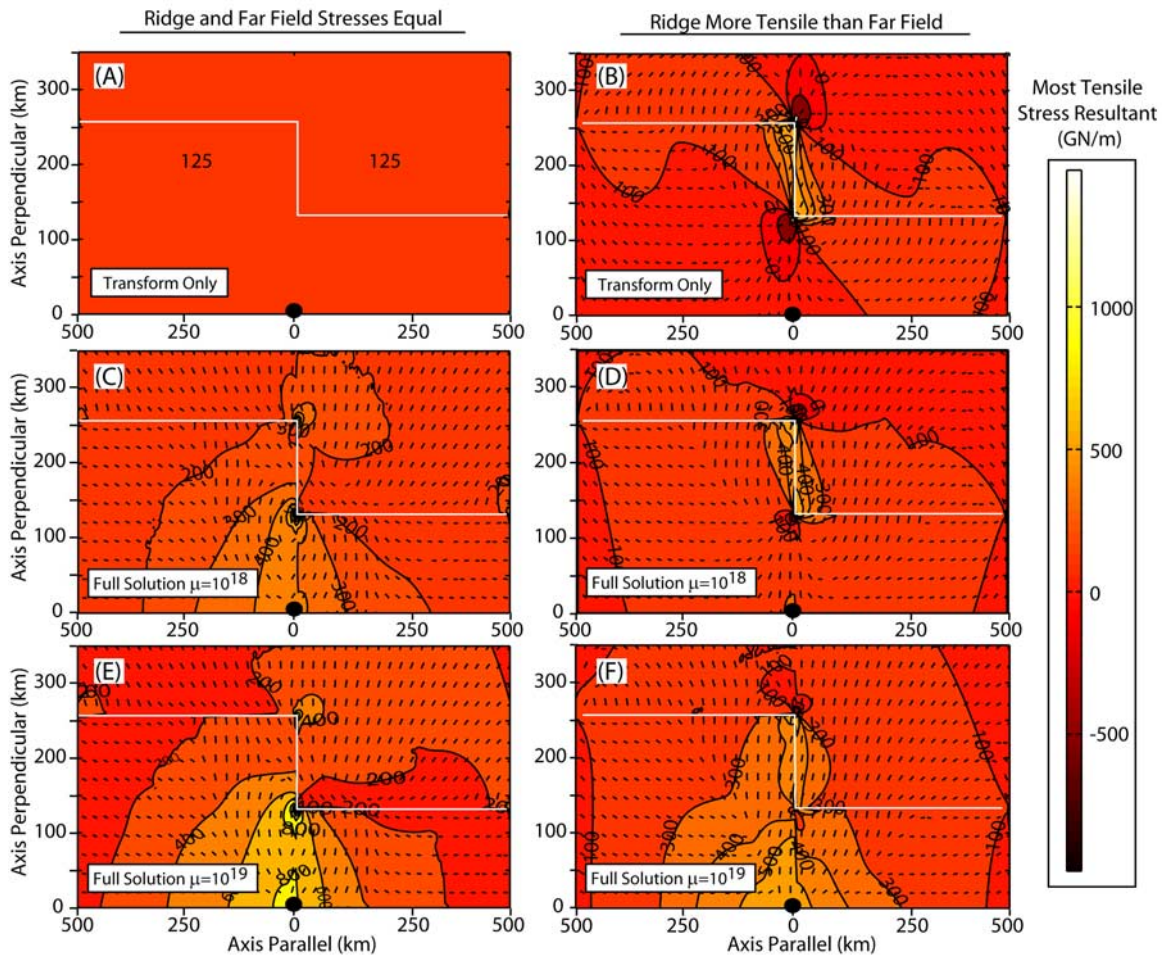


Figure 8. (a) Ridge-transform boundary stresses equal to the isotropic far-field stresses produce an isotropic stress field. (b) Least tensile stress resultant trajectories and magnitudes of most tensile stress resultant due to a segmented ridge show many of the characteristics of the Galápagos lineaments when the ridge is more tensile than the far field by 100 GPa m but do not explain the orientation of the Wolf-Darwin lineament. (c and d) Added effects of a plume with viscosity of 10^{18} Pa s show features consistent with the Galápagos lineaments when the ridge is more tensile than the far field, but deviate near the inside transform corner when the ridge and far-field stresses are equal. (e and f) A plume with a viscosity of 10^{19} Pa s is more consistent with other hot spots, such as Kerguelen. White lines denote the location of the ridge axis, and black dots at the origin denote the model plume center.

shifts to a location close to the plume center with subtle changes in trajectory orientation near the transform (Figure 8f). Overall, the inclusion of the ridge offset maintains the general fan-shaped pattern of least tensile stress trajectories, but deviates from the solution due to a straight ridge near the transform fault where a focus zone is observed.

[32] To assess where volcanic lineaments are most likely to form we divide the predicted stress resultants by the lithospheric yield strength. For both cases with and without a transform, the fraction of the lithospheric yield strength is largest between the model plume center and the ridge axis, where the plate is youngest. To the south of the model plume center the fraction is relatively low (Figures 9b and

9c). Model results therefore show that lineament formation is most likely to occur between the plume and ridge axis in a fan-shaped pattern.

4. Discussion

4.1. Galápagos Lineament Pattern

[33] It is well known that dikes and fractures tend to propagate along trajectories of least tensile stress [Ernst and Buchan, 1997; Glen and Ponce, 2002; Muller et al., 2001; Muller and Pollard, 1977; Ode, 1957; Pollard and Aydin, 1988]. Islands along the lineaments to the west of the southward projection of the 91° W transform fault, display north-northwest trending fractures, whereas east-

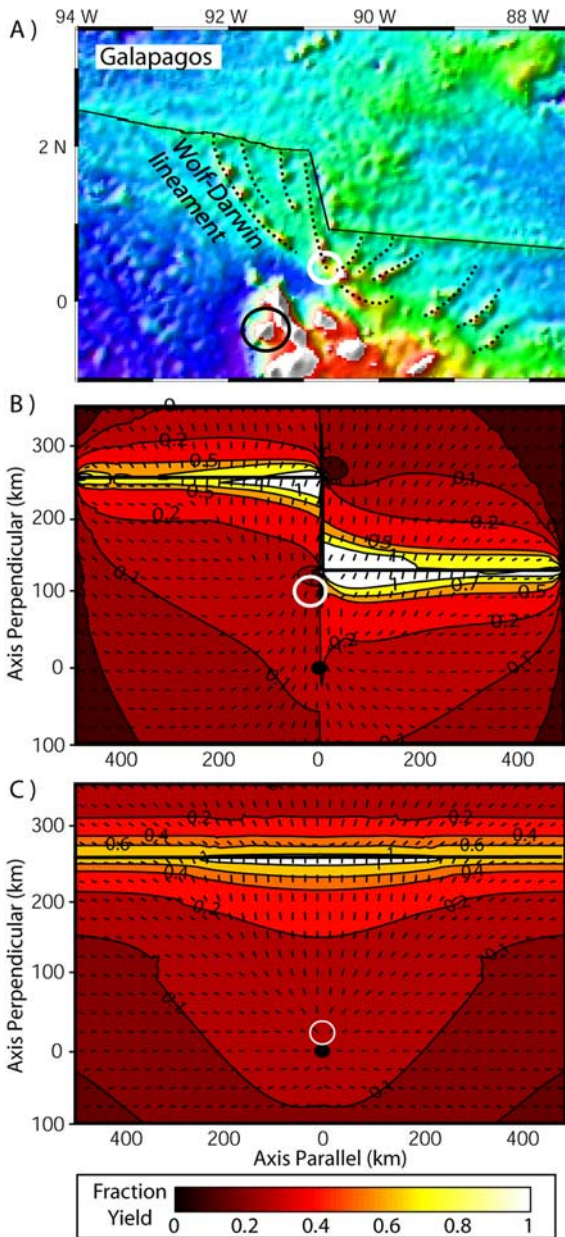


Figure 9. (A) Map of the Galápagos Spreading Center (denoted by subhorizontal black lines), the Galápagos Archipelago (black circle enclosing Fernandina Island, location of most recent volcanism), and the volcanic lineaments (black dashed lines), which appear to fan out from a focus at the white circle. Contours of fraction of lithospheric yield strength (most tensile stress resultant divided by yield strength) for (b) a model with two ridge segments separated by a transform fault and (c) a model with a single, straight ridge axis. Ridges are more tensile than the imposed isotropic far-field stress by 100 GPa m. Ticks mark trajectories of least tension. Magma penetration via dikes will tend to align with these trajectories. Models predict trajectories to fan northward away from an apparent center within the white circles. Black dots show the center of the model mantle plume.

west trending fractures are found to the east [Cullen and McBirney, 1987; Geist et al., 1986; Harpp et al., 2003; Harpp and Geist, 2002]. Thus the fractures roughly parallel the lineaments, consistent with our notion that volcanic lineaments will tend to form along trajectories of least principle tension in the whole lithosphere.

[34] The ridge-transform-ridge configuration of the model shown in Figures 8d and 9b is successful in reproducing the gross pattern of lineaments in the Galápagos region. This model successfully predicts lineaments to focus south of the southern transform-ridge intersection. Because predicted magnitudes of integrated stresses are appreciable fractions of the integrated lithospheric strength only on the youngest lithosphere, models also predict formation of lineaments between the presumed plume center (Fernandina Island) and the GSC. While both the straight and segmented ridge models produce the above general characteristics, the segmented ridge does slightly better because the transform fault causes the apparent focus zone to be north of the plume center more consistent with observations (Figures 8, 9b, and 9c). Without the transform, or for large plume viscosities, the focus center is nearly at the plume center, similar to models that only include plume shear and uplift (Figures 5a and 5b). Models including the transform offset thus provide a solution to the paradox of the lineament focus being offset from the presumed plume center.

[35] The transform fault at 91°W was previously suggested to be the primary control on lineament patterns at the Galápagos [Harpp et al., 2003; Harpp and Geist, 2002]. Our models support a significant contribution from the transform, but models also indicate that the plume effects are important. For example, the model with only the ridge-transform effects predicts least tensile stress trajectories that are nearly perpendicular to the Wolf-Darwin lineament and other lineaments far from the transform fault (Figure 8b). In addition, the transform effects cause relatively compressive deviatoric stress resultants south of the lower transform corner which should inhibit lineament formation. The added plume effects produce trajectories consistent with the Wolf-Darwin lineament and tensile stress resultant magnitudes near the southern transform tip. Overall, the lineament pattern is better modeled by the case of a ridge that is more tensile than the far-field stress. The focus of trajectories is better delineated and trajectories close to the transform closely resemble the linea-

ment orientations. We conclude that the plume effects are critical to the fan-like pattern of Galápagos lineaments far from the transform, while the transform fault effects are important to lineament orientations close to the transform and to locating the focus of the fan ridgeward of the plume center.

[36] On the basis of gravity modeling, *Feighner and Richards* [1994] predict a discontinuity in the effective elastic thickness of the Nazca plate near the Galápagos Archipelago, with lithosphere to the west and south of the Wolf-Darwin lineament more rigid than the lithosphere to the north and east. Lithospheric strength in our models varies both north-south due to plate cooling and east-west across the age discontinuity due to the transform fault. This roughly approximates the proposed strength variations of *Feighner and Richards* [1994], only significantly differing between the transform and the WDL. Tests on the importance of this east-west discontinuity to the overall pattern of stress resultants in our models indicate little change in trajectory orientations or stress resultant magnitudes and suggest that inclusion of the more complex strength variations of *Feighner and Richards* [1994] will not significantly alter the solutions.

[37] This said, it is important to note that where the stress resultant magnitudes are equal to or exceed the integrated lithospheric yield strength, the lithosphere will deform anelastically and its behavior is not represented by our elastic rheology. This applies especially to the inside corner regions of the transform fault model where stress concentrations due to the crack tips may exceed the yield strength of young lithosphere (Figure 9b). We therefore consider our purely elastic models as representing the minimal level of sophistication needed to address the posed problem.

[38] Regarding the source of magma feeding the lineaments, geochemical analysis of lavas from the Wolf-Darwin lineament shows increasing plume chemical influence toward the ridge (e.g., $^{87}\text{Sr}/^{86}\text{Sr}$ from 0.7026–0.7034) [*Harpp and Geist*, 2002]. These chemical variations could be caused by changes in melt composition along an asthenospheric plume channel oriented along the pseudo-fault near Wolf Island or by tapping of plume-contaminated mantle dispersed throughout the region and already processed by melting beneath the GSC [*Harpp and Geist*, 2002]. Our models require a melt source beneath the lineaments and suggest that the lithospheric stress field controls

where and how this melt erupts, but do not require asthenospheric channels to form the lineaments.

[39] We propose a model where the lineaments form in regions of high integrated tension that will promote magma to crack its way through the lithosphere and erupt to initiate a volcanic lineament. The process of diking and volcano loading decreases the integrated tension in the underlying lithosphere and leads to tensile stress concentrations near the ends of the lineament. This will promote new volcanism and lengthening of the lineament in a manner much like a giant crack in the lithosphere. Volcanism initiates where magma supply is high and tension is a large fraction of the lithospheric yield strength near the ridge axis. Volcanism subsequently propagates away from the ridge roughly according to the pre-existing lithospheric stress field. Indeed, along Wolf-Darwin, ages are seen to decrease away from the ridge [*Sinton et al.*, 1996] suggesting that volcanism initiated near the ridge axis and propagated southeast. Volcanic initiation near the ridge axis supports the assertion that regions of high lithospheric yield fraction will be most penetrable by magma. Age dating of the other Galápagos lineaments will provide a further test of this hypothesis.

4.2. Islands of the Galápagos Archipelago

[40] Islands of the Galápagos Archipelago also show aligned fractures [*Darwin*, 1860] and the volcanoes themselves are aligned along rectilinear “Darwinian trends” most readily exhibited by the “J”-shaped Isabela island [*McBirney and Williams*, 1969]. The stresses we have modeled could have influenced the formation of these islands. A similar pattern is displayed by least tensile stress trajectories near the plume center in our straight ridge models and slightly ridgeward of the plume center in models of a segmented ridge with a large viscosity plume (Figures 8e, 8f, and 9c). However, the main islands are larger than the volcanic lineaments and will introduce much larger bending stresses which may have been more important in controlling where adjacent volcanoes form [*Hieronymus and Bercovici*, 2001; *ten Brink*, 1991]. Future studies that incorporate bending into models of plume-lithosphere interaction are needed to better explore the formation of the main Galápagos islands.

4.3. Constraints on the Tectonic Stress Field

[41] The differential stress ($\Delta N = N_{11} - N_{22}$) induced by the combination of plume forces, and

the far-field and ridge boundary conditions controls the orientations of the least-tensile stress trajectories and thus the width of the observed fan-shaped pattern. One quantity that characterizes the shape of the fanning lineaments is the half-width, L , along the ridge axis. Our models show that plume-ridge separation, x_p and the differential stress in the far field strongly influence the value of L and may indicate one reason why patterns of lineaments differ between hot spot localities such as Kerguelen, Tristan de Cuhna and the Galápagos.

[42] With knowledge of L , R_p , and x_p from the Galápagos we can use the predictions of Figure 7 to place first-order constraints on the far-field stress field in the near-GSC lithosphere. Taking measured values for $x_p = 260$ km [Ribe, 1996], $L = 255$ km, and a $R_p = 350$ km based on the location of a distinct decrease in chemical plume influence, crustal thickness and plume-driven melt supply seen at approximately 93°W [Cushman *et al.*, 2004; Detrick *et al.*, 2002], we predict the ratio of differential far-field stress to differential plume stress ($\Delta N_f/|\Delta N_p|$) to fall between -0.2 and 0.1 (Figure 7, gray box). Our models predict a nearly isotropic far-field stress in the near-GSC lithosphere. This estimate provides an independent prediction of the stress field around the Galápagos and provides an additional constraint on lithospheric stress field models.

4.4. Global Lineament Formation

[43] Although the majority of this study focuses on the Galápagos lineaments, volcanic lineaments appear to be common manifestations of hot spot-ridge interaction. We have identified at least 12 separate hot spots currently or previously located near to mid-ocean ridges, showing volcanic lineaments similar to those at the Galápagos. They include Azores, Cobb, Discovery, Foundation, Kerguelen, Line Islands, Louisville, Musicians, Reunion, Sala y Gomez, St. Paul (Amsterdam), and Tristan de Cuhna hot spots. All of the above hot spot-ridge systems share the common characteristic of having a ridge axis near the inferred location of the hot spot based on available dates of volcanism and seafloor magnetic lineations.

[44] Our model predicts plumes to introduce integrated lithospheric stresses of appreciable fractions of lithospheric yield strength only in young lithosphere. To evaluate the off-axis extent of lineament formation we estimate the age of the plate on which the lineaments were emplaced, lineament lengths, and the relative location of the hot spot at

the time of lineament emplacement. Ages of volcanism along the hot spot track and lineaments are compiled from the literature (see Figure 10 for references) and crustal ages are determined from seafloor isochrons [Muller *et al.*, 1997]. We measure the maximum length of lineaments at each hot spot by creating regional bathymetry maps and digitally measuring the distance along each lineament.

[45] Figure 10 shows the relationships between maximum lineament length, plate age and plume-ridge separation for 23 oceanic hot spots with error bars in plume-ridge separation and plate age from the error contours of Muller *et al.* [1997] and errors in lineament length measurements estimated at ± 20 km. Hot spots that do not show evidence for lineaments are given a lineament length of zero. Lineaments, on average, reach lengths of about 75% of the plume-ridge separation distance at the time of emplacement. Approximately linear relationships between lineament length and plate age, and lineament length and plume-ridge separation are seen until a critical distance or seafloor age is reached (Figure 10). Lineaments are not seen beyond 1250 km or in lithosphere older than ~ 25 Ma. This cutoff is likely due to the presence of thick, strong lithosphere resisting plume stresses, the lack of interaction between the ridge and plume at separation >1250 km, or both. Schilling [1991] notes a cutoff in geochemical tracers and bathymetric highs with plume-ridge separations of ~ 1600 km, slightly greater than the maximum distance found in our collection of hot spots with lineaments. In addition, lineaments do not appear to form near ridge-centered plumes. For example, at Iceland volcanic lineaments are primarily focused along 3 major rift axes, but are not present off-axis. This localization of volcanism may be a consequence of efficient suction of magma to these rift zones, or, alternatively, the rift zones themselves may be an expression of a plume-induced stress field similar to that which causes off-axis lineament formation. Not only does Figure 10 demonstrate that lineaments form preferentially within certain plate ages and separation distances, it demonstrates the commonality of lineament formation at near ridge hot spots.

5. Conclusions

[46] In this study we use a 2-D model of plume-ridge interaction to examine factors contributing to the formation of lineaments seen at the Galápagos and other oceanic hot spots. We present a new

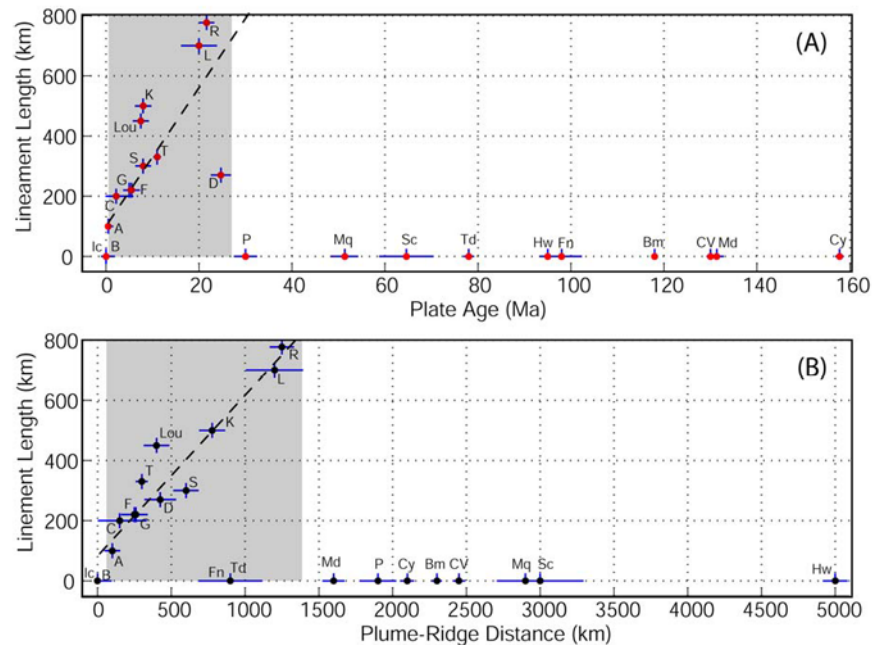


Figure 10. Observations of 23 oceanic hot spots show distinct patterns in lineament formation. (a) This plot of plate age at the time of lineament emplacement versus lineament length demonstrates a region of lineament formation between plate ages of 0.2 and 25 Ma (hot spots without lineaments are associated with a lineament length of zero). (b) Comparison of plume-ridge separation and lineament length also shows a restricted region of formation between 100 and 1250 km. Both trends show an approximately linear (black dotted best fit line) increase in lineament length in the region of formation (gray boxes). Plate ages and errors in plate age from *Muller et al.* [1997]. Where error bars are not visible, the symbol is larger than the error. Hot spots are labeled as follows: A, Amsterdam; B, Bowie; Bm, Bermuda; C, Cobb; CV, Cape Verde; Cy, Canary; D, Discovery; F, Foundation; Fn, Fernando; G, Galápagos; Hw, Hawaii; I, Iceland; K, Kerguelen; L, Line Islands; Lou, Louisville; Md, Madeira; Mq, Marquesas; P, Pitcairn; R, Reunion; S, Sala y Gomez; Sc, Society; T, Tristan; Td, Trinadade. Lineament ages and hot spot tracks are compiled from the literature [*Bonneville et al.*, 1988; *Davis et al.*, 2002; *Desonie and Duncan*, 1990; *Douglass et al.*, 1999; *Duncan*, 1984; *Geldmacher and Hoernle*, 2000; *Geli et al.*, 1998; *Hekinian et al.*, 1999; *O'Connor and Duncan*, 1990; *O'Connor and Roex*, 1992; *O'Connor et al.*, 1995; *Small*, 1995; *Sonne*, 1990; *Vlastelic et al.*, 1998; *Weis et al.*, 2002].

method of simulating patterns of stress caused by the local factors of plume shear, gravitational body forces due to uplifted topography, ridge boundary conditions, and variations in plate thickness.

[47] Least tensile stress trajectories due to a plume interacting with a linear ridge axis form a fan-like pattern between the plume and ridge. The trajectories tend to curve to meet the ridge axis at approximately right angles if the shear stress on the ridge is zero. While the general fan-shaped pattern is preserved beyond plume-ridge separations over ~ 0.5 times the radius of the dominantly axisymmetric plume flow (Figure 6, where $x_p > L$), the pattern deviates to the east and west for smaller plume-ridge separations, but maintains a ridge-perpendicular orientation between the ridge and plume center. The addition of a transform fault creates a more complex pattern with least tensile stress trajectories again curving to meet the ridge at

right angles, but with the focal point of the fan pattern further ridge-ward than the corresponding linear ridge model (Figure 9).

[48] Increasing the far-field tension perpendicular to the ridge relative to that parallel to the ridge causes the width of the fan at the ridge axis to decrease in an approximately quadratic function of ΔN_f . Examination of this relationship in context of Galápagos lineaments suggests that the differential far-field stress resultant is nearly isotropic in the region of the GSC.

[49] Our model stress resultant trajectories closely resemble the pattern of lineaments seen near the Galápagos when the ridge is segmented and more tensile than the far-field stress. Results reconcile the difference in plume center location from that of lineament focus and explain the decreasing trend and curvature of lineaments as the transform is

approached. We propose that the Galápagos lineaments form near the ridge axis where tension is a large fraction of the lithospheric strength and then propagate southward roughly following the predicted stress trajectories. Volcanism is probably fed by a widespread melt supply from the underlying asthenosphere.

[50] Measurements of 23 separate oceanic hot spots show a nearly linear increase in volcanic lineament length with increasing age of the plate at the hot spot and increasing plume-ridge separation distance. This linear relationship holds until plate ages of ~ 25 Ma and plume-ridge separation distances in excess of ~ 1250 km where lineament formation is no longer observed. We conclude that beyond 25 Ma, plate thicknesses are too large for plume stresses to enhance the ability of magma to penetrate the plate. Also, plume-ridge distances greater than 1250 km probably prevent significant asthenospheric interaction of the plume and ridge.

Appendix A

[51] Because the lithosphere is thickening approximately with the square root of distance from the ridge, it accretes in a curved form. As the lateral extent is much larger than its thickness, the lithosphere can be approximated as a thin shell. The shape of a thin shell may be described in terms of two orthogonal coordinates, α and β , which in general are curvilinear [Gould, 1988]. Infinitesimal changes in α and β are related to changes in arc length along the mid plane of the shell, ds_α and ds_β , according to

$$\begin{aligned} ds_\alpha &= A d\alpha, \\ ds_\beta &= B d\beta, \end{aligned} \quad (\text{A1})$$

where A and B are known as Lamé parameters and, for the lithosphere, we define $d\alpha = dx_1$ and $d\beta = dx_2$ (Figure 2). Using this convention, $B = 1$ (no curvature parallel to the ridge) and A is found to be

$$A = \left(1 + \left(\frac{dx_3}{dx_1} \right)^2 \right)^{1/2}, \quad (\text{A2})$$

where dx_3/dx_1 describes the slope of the shell mid-plane. Using this curvilinear geometry, force equilibrium can be described in three orthogonal directions [Gould, 1988]

$$\begin{aligned} [(BN_\alpha)_{,\alpha} + (AN_\beta)_{,\beta} + A_{,\beta}N_\alpha - B_{,\alpha}N_\beta] + Q_\alpha \frac{AB}{R_\alpha} \\ + q_\alpha AB = 0, \end{aligned} \quad (\text{A3})$$

$$\begin{aligned} [(BN_\alpha)_{,\alpha} + (AN_\beta)_{,\beta} + B_{,\beta}N_\alpha - A_{,\alpha}N_\beta] + Q_\beta \frac{AB}{R_\beta} \\ + q_\beta AB = 0, \end{aligned} \quad (\text{A4})$$

$$[(BQ_\alpha)_{,\alpha} + (AQ_\beta)_{,\beta}] - N_\alpha \frac{AB}{R_\alpha} - N_\beta \frac{AB}{R_\beta} + q_n AB = 0, \quad (\text{A5})$$

where partial derivatives are denoted by commas followed by coordinate directions (to be complete we show the terms involving derivatives of B even though they are zero). R_i is the radius of curvature in the i direction, Q_i is depth-integrated transverse shear, and q_i are the loads on the plate. These equilibrium equations are coupled through the transverse shear term, Q_i , which also acts to couple them with the equations of angular momentum.

[52] To simplify equations (A3)–(A5), we determine the appropriate values of the Lamé parameter A and the radii of curvature of the unstressed lithosphere. Assuming the slope of the mid-plane (dx_3/dx_1 , equation (A2)) is parallel to the surface of the lithosphere, radius of curvature may be described by seafloor deepening due to plate cooling away from the ridge [Stein and Stein, 1992]

$$z = 2.60 + c\sqrt{x_1}, \quad (\text{A6})$$

where $c = \frac{0.365}{\sqrt{u}}$, u is the seafloor spreading rate, and x_1 is the distance from the ridge. Thus equation (A2) becomes

$$A = \left(1 + \left(\frac{c^2}{4x_1} \right) \right)^{(1/2)}. \quad (\text{A7})$$

For $u = 30$ km/myr and $x_1 = 10$ – 100 km off axis, $(c^2/4x_1)$ is of order 10^{-4} to 10^{-5} so A is very close to 1.

[53] The radius of curvature in the ridge parallel direction, R_β , is infinite because we assume all curvature is parallel to plate spreading and radius of curvature due to uplift is large. The radius of curvature perpendicular to the ridge axis is

$$R_\alpha = \frac{\left[1 + \left(\frac{dx_3}{dx_1} \right)^2 \right]^{(3/2)}}{\frac{d^2x_3}{dx_1^2}}. \quad (\text{A8})$$

Again using $u = 30$ km/myr and $x_1 = 10$ km, the radius of curvature near the ridge (0.33 m.y. old crust) is found to be $R_\alpha > \sim 1900$ km. We expect the stress resultant terms in (A3)–(A5) to be of order N_{ij}/R_p , where $R_p \sim 10^2$ km is the character-

istic radial extent that plume forces, q_i , act on the plate. Since $R_\alpha \gg R_p$, the terms involving R_α^{-1} (and R_β^{-1}) in (A3)–(A5) are negligible and the resulting linear momentum equations have a form similar to those of plane stress (with $A = B = 1$)

$$[(N_{\alpha})_{,\alpha} + (N_{\beta\alpha})_{,\beta}] + q_\alpha = 0, \quad (\text{A9})$$

$$[(N_{\alpha\beta})_{,\alpha} + (N_\beta)_{,\beta}] + q_\beta = 0. \quad (\text{A10})$$

We use these equations of equilibrium to formulate our model of plume-ridge interaction.

Appendix B

[54] To derive the governing equation for a plate with thickness, h , that varies laterally, the constitutive equations (equation (3)) are substituted into the equilibrium (equation (2)) equations to yield

$$\frac{Eh}{(1-\nu^2)} \left[\frac{\partial \varepsilon_{11}}{\partial x_1} + \nu \frac{\partial \varepsilon_{22}}{\partial x_1} \right] + \frac{Eh}{(1+\nu)} \frac{\partial \varepsilon_{12}}{\partial x_2} = - \left[q_1 + \frac{\partial h}{\partial x_1} \frac{N_{11}}{h} + \frac{\partial h}{\partial x_2} \frac{N_{12}}{h} \right] = b_1, \quad (\text{B1})$$

$$\frac{Eh}{(1-\nu^2)} \left[\frac{\partial \varepsilon_{22}}{\partial x_2} + \nu \frac{\partial \varepsilon_{11}}{\partial x_2} \right] + \frac{Eh}{(1+\nu)} \frac{\partial \varepsilon_{12}}{\partial x_1} = - \left[q_2 + \frac{\partial h}{\partial x_2} \frac{N_{22}}{h} + \frac{\partial h}{\partial x_1} \frac{N_{12}}{h} \right] = b_2, \quad (\text{B2})$$

and compatibility (equation (4)) equation to yield

$$(1-\nu) \left[\frac{\partial^2 \frac{N_{11}}{h}}{\partial x_2^2} + \frac{\partial^2 \frac{N_{22}}{h}}{\partial x_1^2} \right] - \nu \left[\frac{\partial^2 \frac{N_{22}}{h}}{\partial x_2^2} + \frac{\partial^2 \frac{N_{11}}{h}}{\partial x_1^2} \right] = 2 \frac{\partial^2 \frac{N_{12}}{h}}{\partial x_1 \partial x_2}. \quad (\text{B3})$$

Terms with gradients in thickness are placed on the right hand side (r.h.s.) of equations (B1) and (B2) and are grouped as “fictitious” body forces into new variables, b_1 and b_2 , which also include the effects of plume shear and uplift (q_1 and q_2 ; see equation (9)). Formulation of the governing equation is achieved by combining the compatibility and equilibrium equations as is commonly done in elasticity theory. To facilitate this, derivatives of equations (B1) and (B2) are taken in the 1 and 2 directions, respectively, and the resulting equations are summed:

$$-\frac{\partial^2 \frac{N_{11}}{h}}{\partial x_1^2} - \frac{\partial^2 \frac{N_{22}}{h}}{\partial x_2^2} - \left(\frac{\partial \frac{b_1}{h}}{\partial x_1} + \frac{\partial \frac{b_2}{h}}{\partial x_2} \right) = 2 \frac{\partial^2 \frac{N_{12}}{h}}{\partial x_1 \partial x_2}. \quad (\text{B4})$$

Now we may solve for the general governing equation for an elastic plate of varying thickness by equating the r.h.s. of (B4) and (B3) and simplifying

$$\nabla^2(\bar{\sigma}_{11} + \bar{\sigma}_{22}) = -\frac{1}{(1-\nu)} \left[\frac{\partial b_1}{\partial x_1} + \frac{\partial b_2}{\partial x_2} \right]. \quad (\text{B5})$$

The governing equation relates the change in depth-averaged stresses ($\bar{\sigma}_{ij} = N_{ij}/h$) in a plate of varying thickness to the imposed loads (q_i), subject to specified (ridge axis) boundary conditions. The form of (B5) is identical in form to the governing equation for plane stress and allows the solution to be determined through the use of an Airy stress function method. Because the final value of the “fictitious” body force terms depend on the stress resultants, the equations are solved iteratively.

Acknowledgments

[55] The authors would like to thank S. Martel for providing the 2-D boundary element code used in portions of this study. We would also like to thank N. Ribe for discussions about the method used and A. Delorey, M. Behn, A. Oakley, and S. Martel for helpful comments on previous versions of this manuscript. Thoughtful reviews were provided by D. Graham, M. Richards, and R. Buck which helped strengthen the manuscript. Maps were made using GMT version 3.4.2 by P. Wessel and W. F. Smith. Mittelstaedt and Ito were funded by NSF grants OCE03-7051 and OCE03-51234 and Ito’s start-up money from SOEST. The computer cluster used for the computations was funded with NSF grant OCE01-36793. This is SOEST contribution 6545.

References

- Barber, J. R. (2002), *Elasticity*, pp. 185–187, Springer, New York.
- Behn, M. D., J. Lin, and M. T. Zuber (2002), Evidence for weak oceanic transform faults, *Geophys. Res. Lett.*, *29*(24), 2207, doi:10.1029/2002GL015612.
- Bonneville, A., J. P. Barriot, and R. Bayer (1988), Evidence from geoid data of a hotspot origin for the Southern Mascarene Plateau and Mascarene Islands (Indian Ocean), *J. Geophys. Res.*, *93*(B5), 4199–4212.
- Buck, W. R., and A. N. B. Poliakov (1998), Abyssal hills formed by stretching oceanic lithosphere, *Nature*, *392*, 272–275.
- Canales, J. P., J. J. Dañobeitia, R. S. Detrick, E. E. E. Hooft, R. Bartolomé, and D. F. Naar (1997), Variations in axial morphology along the Galápagos spreading center and the influence of the Galápagos hotspot, *J. Geophys. Res.*, *102*(B12), 27,341–27,354.
- Chen, Y., and W. J. Morgan (1990), A nonlinear rheology model for mid-ocean ridge axis topography, *J. Geophys. Res.*, *95*(B11), 17,583–17,604.
- Coffin, M. F., M. S. Pringle, R. A. Duncan, T. P. Gladczenko, M. Storey, R. D. Muller, and L. A. Gahagan (2002), Kerguelen hotspot magma output since 130 Ma, *J. Petrol.*, *43*(7), 1121–1139.
- Crouch, S. L., and A. M. Starfield (1983), *Boundary Element Methods in Solid Mechanics: With Applications in Rock*

- Mechanics and Geological Engineering*, pp. 45–47, Allen and Unwin, St Leonards, NSW, Australia.
- Cullen, A., and A. R. McBirney (1987), The volcanic geology and petrology of Isla Pinta, Galapagos archipelago, *Geol. Soc. Am. Bull.*, *98*, 294–301.
- Cushman, B., J. Sinton, G. Ito, and J. Eaby Dixon (2004), Glass compositions, plume-ridge interaction, and hydrous melting along the Galápagos Spreading Center, 90.5°W to 98°W, *Geochem. Geophys. Geosyst.*, *5*, Q08E17, doi:10.1029/2004GC000709.
- Darwin, C. (1860), *The Voyage of the Beagle*, Penguin USA, East Rutherford, N. J.
- Davis, A. S., L. B. Gray, D. A. Clague, and J. R. Hein (2002), The Line Islands revisited: New ⁴⁰Ar/³⁹Ar geochronologic evidence for episodes of volcanism due to lithospheric extension, *Geochem. Geophys. Geosyst.*, *3*(3), 1018, doi:10.1029/2001GC000190.
- Desonie, D. L., and R. A. Duncan (1990), The Cobb-Eickelberg Seamount Chain: Hotspot volcanism with mid-ocean ridge basalt affinity, *J. Geophys. Res.*, *95*(B8), 12,697–12,711.
- Detrick, R. S., J. M. Sinton, G. Ito, J. P. Canales, M. Behn, T. Blacic, B. Cushman, J. E. Dixon, D. W. Graham, and J. J. Mahoney (2002), Correlated geophysical, geochemical, and volcanological manifestations of plume-ridge interaction along the Galápagos Spreading Center, *Geochem. Geophys. Geosyst.*, *3*(10), 8501, doi:10.1029/2002GC000350.
- Douglass, J., J. Schilling, and D. Fontignie (1999), Plume-ridge interactions of the Discovery and Shona mantle plumes with the southern Mid-Atlantic Ridge (40°–55°S), *J. Geophys. Res.*, *104*(B2), 2941–2962.
- Duncan, R. A. (1984), Age progressive volcanism in the New England Seamounts and the opening of the central Atlantic Ocean, *J. Geophys. Res.*, *89*(B12), 9980–9990.
- Dyment, J. (1998), Evolution of the Carlsberg Ridge between 60 and 45 Ma: Ridge propagation, spreading asymmetry, and the Deccan-Reunion hotspot, *J. Geophys. Res.*, *103*, 24,067–24,084.
- Ernst, R. E., and K. L. Buchan (1997), Giant radiating dyke swarms: Their use in identifying pre-Mesozoic large igneous provinces and mantle plumes, in *Large Igneous Provinces: Continental, Oceanic, and Planetary Flood Volcanism*, *Geophys. Monogr. Ser.*, vol. 100, edited by J. Mahoney and M. F. Coffin, pp. 297–333, AGU, Washington, D. C.
- Feighner, M. A., and M. A. Richards (1994), Lithospheric structure and compensation mechanisms of the Galapagos Archipelago, *J. Geophys. Res.*, *99*(B4), 6711–6729.
- Forsyth, D., and S. Uyeda (1975), On the relative importance of the driving forces of plate motion, *Geophys. J. R. Astron. Soc.*, *43*, 163–200.
- Geist, D., A. R. McBirney, and R. A. Duncan (1986), Geology and petrogenesis of lavas from San Cristobal Island, Galapagos Archipelago, *Geol. Soc. Am. Bull.*, *97*, 555–566.
- Geist, D., W. White, T. Naumann, and R. Reynolds (1999), Illegitimate magmas of the Galapagos: Insights into mantle mixing and magma transport, *Geology*, *27*(12), 1103–1106.
- Geldmacher, J., and K. Hoernle (2000), The 72 Ma geochemical evolution of the Madeira hotspot (eastern North Atlantic): Recycling of Paleozoic (<500 Ma) oceanic lithosphere, *Earth Planet. Sci. Lett.*, *183*, 73–92.
- Geli, L., D. Aslanian, J. Olivet, I. Vlastelic, L. Dosso, H. Guillou, and H. Bougault (1998), Location of the Louisville hotspot and origin of Hollister Ridge: Geophysical constraints, *Earth Planet. Sci. Lett.*, *164*, 31–40.
- Glen, J. M. G., and D. A. Ponce (2002), Large-scale fractures related to inception of the Yellowstone hotspot, *Geology*, *30*(7), 647–650.
- Gould, P. L. (1988), *Analysis of Shells and Plates*, Springer, New York.
- Gudmundsson, A. (1995), Stress fields associated with oceanic transform faults, *Earth Planet. Sci. Lett.*, *136*, 603–614.
- Hanan, B. B., R. H. Kingsley, and J.-G. Schilling (1986), Pb isotope evidence in the South Atlantic for migrating ridge-hotspot interactions, *Nature*, *322*, 137–144.
- Hanan, B. B., J. Blichert-Toft, R. Kingsley, and J. Schilling (2000), Depleted Iceland mantle plume geochemical signature: Artifact of multicomponent mixing?, *Geochem. Geophys. Geosyst.*, *1*(4), doi:10.1029/1999GC000009.
- Hardarson, B. S., J. G. Fitton, R. M. Ellam, and M. S. Pringle (1997), Rift relocation—A geochemical and geochronological investigation of a paleo-rift in northwest Iceland, *Earth Planet. Sci. Lett.*, *153*, 181–196.
- Harpp, K., and D. Geist (2002), Wolf-Darwin lineament and plume-ridge interaction in northern Galápagos, *Geochem. Geophys. Geosyst.*, *3*(11), 8504, doi:10.1029/2002GC000370.
- Harpp, K. S., D. J. Fornari, D. J. Geist, and M. D. Kurz (2003), Genovesa Submarine Ridge: A manifestation of plume-ridge interaction in the northern Galápagos Islands, *Geochem. Geophys. Geosyst.*, *4*(9), 8511, doi:10.1029/2003GC000531.
- Hekinian, R., P. Stoffers, D. Ackermann, S. Revillon, M. Maia, and M. Bohn (1999), Ridge-hotspot interaction: The Pacific-Antarctic Ridge and the foundation seamounts, *Mar. Geol.*, *160*, 199–223.
- Hieronimus, C. F., and D. Bercovici (2001), A theoretical model of hotspot volcanism: Control on volcanic spacing and patterns via magma dynamics and lithospheric stresses, *J. Geophys. Res.*, *106*(B1), 683–702.
- Huppert, H. (1982), The propagation of two-dimensional and axisymmetric viscous gravity currents over a rigid horizontal surface, *J. Fluid Mech.*, *121*, 43–58.
- Ito, G., and J. Lin (1995), Oceanic spreading center-hotspot interactions: Constraints from along-isochron bathymetric and gravity anomalies, *Geology*, *23*, 657–660.
- Ito, G., J. Lin, and C. W. Gable (1997), Interaction of mantle plumes and migrating mid-ocean ridges: Implications for the Galapagos plume-ridge system, *J. Geophys. Res.*, *102*(B7), 15,403–15,417.
- Ito, G., J. Lin, and D. Graham (2003), Observational and theoretical studies of the dynamics of mantle plume–mid-ocean ridge interaction, *Rev. Geophys.*, *41*(4), 1017, doi:10.1029/2002RG000117.
- Keller, R. A., M. R. Fisk, and W. M. White (2000), Isotopic evidence for Late Cretaceous plume-ridge interaction at the Hawaiian hotspot, *Nature*, *405*, 673–676.
- Kopp, H., C. Kopp, J. Phipps Morgan, E. R. Flueh, W. Weinrebe, and W. J. Morgan (2003), Fossil hot spot-ridge interaction in the Musicians Seamount Province: Geophysical investigations of hot spot volcanism at volcanic elongated ridges, *J. Geophys. Res.*, *108*(B3), 2160, doi:10.1029/2002JB002015.
- Lonsdale, P. (1988), Geography and history of the Louisville Hotspot Chain in the southwest Pacific, *J. Geophys. Res.*, *93*(B4), 3078–3104.
- McBirney, A. R., and H. Williams (1969), *Geology and Petrology of the Galapagos Islands*, Geol. Soc. Am., Boulder, Colo.
- Morgan, W. J. (1978), Rodriguez, Darwin, Amsterdam... A second type of hotspot island, *J. Geophys. Res.*, *83*(B11), 5355–5360.

- Muller, J. R., G. Ito, and S. J. Martel (2001), Effects of volcano loading on dike propagation in an elastic half-space, *J. Geophys. Res.*, *106*(B6), 11,101–11,113.
- Muller, O., and D. Pollard (1977), The state of stress near Spanish Peaks, Colorado, determined from a dike pattern, *Pure Appl. Geophys.*, *115*, 69–86.
- Muller, R. D., W. R. Roest, J. Royer, and L. A. Gahagan (1997), Digital isochrons of the world's ocean floor, *J. Geophys. Res.*, *102*(B2), 3211–3214.
- Muller, R. D., W. R. Roest, and J. Royer (1998), Asymmetric sea-floor spreading caused by ridge-plume interactions, *Nature*, *396*, 455–459.
- Nadin, P. A., N. J. Kusznir, and J. Toth (1995), Transient regional uplift in the Early Tertiary of the northern North Sea and the development of the Iceland Plume, *J. Geol. Soc. London*, *152*, 953–958.
- Novozhilov, V. V. (1959), *The Theory of Thin Shells*, 376 pp., Springer, New York.
- O'Connor, J. M., and R. A. Duncan (1990), Evolution of the Walvis Ridge–Rio Grande rise hot spot system: Implications for African and South American plate motions over plumes, *J. Geophys. Res.*, *95*(B11), 17,475–17,502.
- O'Connor, J. M., and A. P. Roex (1992), South Atlantic hot spot-plume systems: 1. Distribution of volcanism in time and space, *Earth Planet. Sci. Lett.*, *113*, 343–364.
- O'Connor, J. O., P. Stoffers, and M. O. McWilliams (1995), Time-space mapping of Easter Chain volcanism, *Earth Planet. Sci. Lett.*, *136*, 195–212.
- Ode, H. (1957), Mechanical analysis of the dike pattern of the Spanish Peaks area, Colorado, *Geol. Soc. Am. Bull.*, *68*, 567–576.
- Olson, P. (1990), Hot spots, swells and mantle plumes, in *Magma Transport and Storage*, edited by M. P. Ryan, pp. 33–51, John Wiley, Hoboken, N. J.
- Parsons, B., and J. G. Sclater (1977), An analysis of the variation of ocean floor bathymetry and heat flow with age, *J. Geophys. Res.*, *82*, 803–827.
- Pollard, D. D., and A. Aydin (1984), Propagation and linkage of oceanic ridge segments, *J. Geophys. Res.*, *89*, 10,017–10,028.
- Pollard, D., and A. Aydin (1988), Progress in understanding jointing over the past century, *Geol. Soc. Am. Bull.*, *100*, 1181–1204.
- Ribe, N. M. (1996), The dynamics of plume-ridge interaction 2: Off-ridge plumes, *J. Geophys. Res.*, *101*(B7), 16,195–16,204.
- Ribe, N. M., and W. L. Delattre (1998), The dynamics of plume-ridge interaction 3: The effects of ridge migration, *Geophys. J. Int.*, *133*, 511–518.
- Richards, M. A., B. H. Hager, and N. Sleep (1988), Dynamically supported geoid highs over hotspots: Observation and theory, *J. Geophys. Res.*, *93*(B7), 7690–7708.
- Schilling, J.-G. (1991), Fluxes and excess temperatures of mantle plumes inferred from their interaction with migrating mid-ocean ridges, *Nature*, *352*, 397–403.
- Schilling, J., D. Fontignie, J. Blichert-Toft, R. Kingsley, and U. Tomza (2003), Pb-Hf-Nd-Sr isotope variations along the Galápagos Spreading Center (101°–83°W): Constraints on the dispersal of the Galápagos mantle plume, *Geochem. Geophys. Geosyst.*, *4*(10), 8512, doi:10.1029/2002GC000495.
- Schubert, G., and R. N. Hey (1986), Mantle viscosity beneath the Galapagos 95.5°W propagating rift, *Geophys. Res. Lett.*, *13*(4), 329–332.
- Shaw, W. J., and J. Lin (1996), Models of ocean ridge lithospheric deformation: Dependence on crustal thickness, spreading rate, and segmentation, *J. Geophys. Res.*, *101*(B8), 17,977–17,993.
- Sinton, C. W., D. M. Christie, and R. A. Duncan (1996), Geochronology of Galapagos Seamounts, *J. Geophys. Res.*, *101*(B6), 13,689–13,700.
- Sinton, J. M. (1992), Mid-ocean ridge magma chambers, *J. Geophys. Res.*, *97*, 197–216.
- Sinton, J., R. Detrick, J. P. Canales, G. Ito, and M. Behn (2003), Morphology and segmentation of the western Galápagos Spreading Center, 90.5°–98°W: Plume-ridge interaction at an intermediate spreading ridge, *Geochem. Geophys. Geosyst.*, *4*(12), 8515, doi:10.1029/2003GC000609.
- Small, C. (1995), Observations of ridge-hotspot interactions in the Southern Ocean, *J. Geophys. Res.*, *100*, 17,931–17,946.
- Smith, W. H. F., and D. T. Sandwell (1997), Global seafloor topography from satellite altimetry and ship depth soundings, *Science*, *277*, 1957–1962.
- Sonne, F. S. (1990), Active Pitcairn hotspot found, *Mar. Geol.*, *95*, 51–55.
- Stein, C. A., and S. Stein (1992), A model for the global variation in oceanic depth and heat flow with lithospheric age, *Nature*, *359*, 123–129.
- Taylor, R. N., B. J. Murton, and M. F. Thirwall (1995), Petrographic and geochemical variation along the Reykjanes Ridge, 57°N–59°N, *J. Geol. Soc. London*, *152*, 1031–1037.
- ten Brink, U. (1991), Volcano spacing and plate rigidity, *Geology*, *19*, 397–400.
- Timoshenko, S. P., and J. N. Goodier (1934), *Theory of Elasticity*, pp. 127–132, McGraw-Hill, New York.
- Vlastelic, I., L. Dosso, H. Guillou, H. Bougault, L. Geli, J. Etoubleau, and J. L. Joron (1998), Geochemistry of the Hollister Ridge: Relation with the Louisville hotspot and the Pacific-Antarctic Ridge, *Earth Planet. Sci. Lett.*, *160*, 777–793.
- Weis, D., F. A. Frey, R. Schlich, M. Schaming, R. Montigny, D. Damasceno, N. Mattielli, K. E. Nicolaysen, and J. S. Scoates (2002), Trace of the Kerguelen mantle plume: Evidence from seamounts between the Kerguelen Archipelago and Heard Island, Indian Ocean, *Geochem. Geophys. Geosyst.*, *3*(6), 1033, doi:10.1029/2001GC000251.
- Werner, R., K. Hoernle, U. Barckhausen, and F. Hauff (2003), Geodynamic evolution of the Galápagos hot spot system (Central East Pacific) over the past 20 m.y.: Constraints from morphology, geochemistry, and magnetic anomalies, *Geochem. Geophys. Geosyst.*, *4*(12), 1108, doi:10.1029/2003GC000576.
- Wessel, P., and L. W. Kroenke (1998), The geometric relationship between hot spots and seamounts: Implications for Pacific hot spots, *Earth Planet. Sci. Lett.*, *158*, 1–18.
- Westaway, R. (1993), Forces associated with mantle plumes, *Earth Planet. Sci. Lett.*, *119*, 331–348.
- White, R., D. McKenzie, and K. O'Nions (1992), Oceanic crustal thickness from seismic measurements and rare earth element inversions, *J. Geophys. Res.*, *97*(B13), 19,683–19,715.
- White, W. M., A. R. McBirney, and R. A. Duncan (1993), Petrology and geochemistry of the Galapagos Islands: Portrait of a pathological mantle plume, *J. Geophys. Res.*, *98*(B11), 19,533–19,563.
- Wilson, D. S., and R. N. Hey (1995), History of rift propagation and magnetization intensity for the Cocos-Nazca spreading center, *J. Geophys. Res.*, *100*(B7), 10,041–10,056.